

Modular Self-Reconfigurable Continuum Robot for General Purpose Loco-Manipulation

Yilin Cai , Haokai Xu, Yifan Wang , *Graduate Student Member, IEEE*, Desai Chen , Wojciech Matusik , Wan Shou , and Yue Chen , *Member, IEEE*

Abstract—Modular Self-Reconfigurable Robots offer exceptional adaptability and versatility through reconfiguration, but traditional rigid robot designs lack the compliance necessary for effective interaction with complex environments. Recent advancements in modular soft robots address this shortcoming with enhanced flexibility; however, their designs lack the capability of active self-reconfiguration and heavily rely on manual assembly. In this letter, we present a modular self-reconfigurable soft continuum robotic system featuring a continuum backbone and an omnidirectional docking mechanism. This design enables each module to independently perform loco-manipulation and self-reconfiguration. We then propose a kinetostatic model and conduct a geometrical docking range analysis to characterize the robot's performance. The reconfiguration process and the distinct motion gait for each configuration are also developed, including rolling, crawling, and snake-like undulation. Experimental demonstrations show that both single and multiple connected modules can achieve successful loco-manipulation, adapting effectively to various environments.

Index Terms—Continuum robot, loco-manipulation, modular robot, self-reconfiguration.

I. INTRODUCTION

MODULAR Self-Reconfigurable Robots (MSRRs) have attracted significant attentions because of their unique ability to reconfigure into various shapes, offering

Received 31 August 2024; accepted 19 December 2024. Date of publication 6 January 2025; date of current version 17 January 2025. This article was recommended for publication by Associate Editor K. H. Petersen and Editor M. A. Hsieh upon evaluation of the reviewers' comments. This work was supported in part by the NSF CAREER Award under Grant 2339202 and in part by the USDA-NIFA's National Robotics Initiative Award under Grant 2022-11065 in collaboration with the National Science Foundation. (*Corresponding author: Yue Chen*.)

Yilin Cai and Yifan Wang are with the Department of Mechanical Engineering, Georgia Institute of Technology, Atlanta, GA 30332 USA (e-mail: yilincai@gatech.edu; wangyf@gatech.edu).

Haokai Xu is with the Department of Electrical and Computer Engineering, Georgia Institute of Technology, Atlanta, GA 30332 USA (e-mail: hxu464@gatech.edu).

Desai Chen is with Inkbit Inc., Medford, MA 02155 USA (e-mail: dchen@inkbit3d.com).

Wojciech Matusik is with the Computer Science and Artificial Intelligence Laboratory, Massachusetts Institute of Technology, Cambridge, MA 02139 USA (e-mail: wojciech@csail.mit.edu).

Wan Shou is with the Department of Mechanical Engineering, University of Arkansas, Fayetteville, AR 72701 USA (e-mail: wshou@uark.edu).

Yue Chen is with the Department of Biomedical Engineering, Georgia Institute of Technology / Emory University, Atlanta, GA 30332 USA (e-mail: yue.chen@bme.gatech.edu).

The design is open sourced at <https://missinglight.github.io/assets/project/msrcr.html>.

This letter has supplementary downloadable material available at <https://doi.org/10.1109/LRA.2025.3526560>, provided by the authors.

Digital Object Identifier 10.1109/LRA.2025.3526560

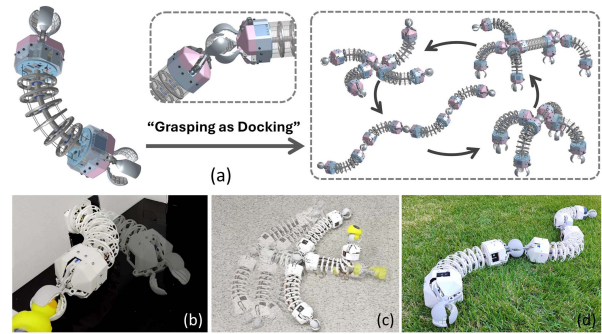


Fig. 1. Overview of the modular self-reconfigurable continuum robot. (a) Module docking through grasping and self-reconfiguration between morphologies. (b-d) Robotic manipulation and locomotion in diverse environments.

unprecedented adaptability for performing diverse tasks. This adaptability allows them to respond effectively to diverse operation scenarios by changing into different robot morphologies or mimicking different biological structures [1], [2].

However, existing reconfigurable robotic systems have mainly utilized rigid articulated modules composed of simple geometric shapes such as balls, tetrahedrons, or cuboids [3]. These rigid modules have limited capabilities for locomotion and manipulation in 3D space, requiring a large number of them with increased control complexity for task execution. In addition, rigid-bodied reconfigurable robots lack the inherent compliance necessary to effectively interact with or adapt to complicated terrains and unstructured environments, which also restricts their ability to replicate agile movements observed in biological systems. Recent studies in modular soft robots [4], [5], [6] have shown a growing trend in addressing this challenge. With inherent compliance, modular soft robots have achieved a wide range of morphologies and functionalities, such as locomotion (e.g. walking [4], rolling [7], crawling [8]), manipulation [9], reconfiguration [6], or combinations of these tasks [10]. However, most modular soft robotic systems have not achieved loco-manipulation — the ability to seamlessly integrate locomotion and manipulation in one single coordinated task. A key reason is that these robots often require manual assembly and lack the capability for active on-site self-reconfiguration, restricting their capacity to adapt dynamically to diverse tasks and environments. To enable self-reconfiguration in modular soft robots, key challenges lie in the lack of (1) efficient actuation mechanisms that allow for a fully self-contained system with untethered power source, and (2) efficient docking mechanisms for automatic assembly and disassembly.

In this letter, we propose an untethered Modular Self-Reconfigurable Continuum Robot (MSRCR) for

general-purpose loco-manipulation (Fig. 1). The proposed design provides each module with independent locomotion and manipulation capabilities and enables the system to reconfigure itself by connecting/disconnecting modules without manual assistance. The main contributions of this letter are threefold:

- 1) The design of a modular soft continuum robot that performs single and multi-module locomotion and manipulation, as well as self-configuration between different morphologies.
- 2) An omnidirectional docking mechanism based on the concept of “Grasping as Docking” that facilitates module connection and object manipulation simultaneously.
- 3) The development of distinct motion gaits across various configurations, along with the reconfiguration processes between these configurations.

II. RELATED WORK

A. Rigid Modular Self-Reconfigurable Robots

Traditional MSRRs are mostly made of articulated rigid structures, whose structural components mainly include actuators and connectors [11]. Various actuator designs have been developed to enable modular robots to independently move in the space (SMORES-EP [12], TRADY [13]) or adjust the relative position and orientation between connectors [14]. In terms of connector design, monogamous connectors enable strong one-to-one connections among modules using mechanical (Mori [15], RoomBot [16]) or magnetic mechanisms (M-Block [17], ModQuad [18]). Recent research has shifted towards polygamous connectors for one-to-many free-form connections (FreeBot [19], SnailBOT [20], FireAntV3 [21]).

Despite years of effort in developing various MSRRs, significant challenges remain in enhancing the module’s individual mobility, ensuring stability and adaptability of connectors, and reducing the number of modules required for high scalability.

B. Modular and Reconfigurable Soft Robot

Onal and Rus [7] were among the first to introduce modularization into soft robots, providing a rapid fabrication and repair method for multifunctional soft robots. Following that, one of the main research focuses has been the development of modular soft actuators for assembly into robot arms [22], [23], grippers [24], and locomotion systems [25], [26]. These soft modules serve as a replacement for traditional rigid links and joints to generate continuous, compliant deformation for more complex motions. However, their fixed arrangement typically restrict them to a single function or specific application, limiting their ability to perform dexterous loco-manipulation.

Different from fixed-morphology robotic systems, reconfigurable soft robots can achieve diverse functionalities through different arrangements of modular units [27]. For example, using the same pneumatic muscle actuator unit, quadrupedal [28], tetrahedral [29], snake-like [30] locomotion and even grippers [31] were successfully developed. However, these modules are not designed for independent movement, thus requiring additional customized connectors with increased structural complexity and manual assembly.

C. Self-Reconfigurable Soft Robot

Self-reconfigurable soft robots can autonomously transform their morphologies to adapt to different environments or tasks.

Zou et al. [6] demonstrated the automatic assembly of two soft modular robot arrays inspired by caterpillar locomotion. However, the use of permanent magnets for connection does not allow for controlled self-disassembly. Zhao et al. [32] presented StarBlocks, a soft modular block capable of self-assembly. However, the tethered design and difficulties in disassembling the magnet-based connector add inefficiency in real deployment. Despite these efforts, few studies have successfully developed soft modules capable of efficient self-reconfiguration, primarily due to challenges in achieving effective loco-manipulation and robust docking mechanisms.

III. MSRCR DESIGN

The proposed MSRCR module design (Fig. 2(a) & (b)) features two key components: a soft continuum unit and two docking mechanisms based on hybrid soft-rigid spherical grippers. The design goals of the MSRCR system are to (1) provide high motion dexterity for single module, (2) achieve polygamous omnidirectional docking, and thus (3) enabling both locomotion and manipulation in single module. To meet these goals, the tendon-driven continuum unit will provide 2 Degrees-of-freedom (DoF) bending for compliant locomotion while the spherical grippers allow both the connection between multiple modules and object manipulation. The mechanical design, electronic system and the specifications of the proposed implementation are summarized in this section.

A. Soft Continuum Unit Design

The soft continuum unit aims to provide the spatial DoF of the MSRCR system, which is defined as the module’s independent DoFs for movements such as changing its position and attitude in space [11]. A soft continuum unit can achieve these movements by active bending. This allows the single module to morph its shape and provide non-uniform interactions with the environment, which usually requires more than one module to achieve in rigid systems. Commonly used silicone-based pneumatic-driven actuators require air hoses, pumps and valves, limiting its motion versatility as well as increasing size, weight, and power consumption. Therefore, we choose the tendon-driven soft continuum unit for its low-cost and compact actuation system.

As shown in Fig. 2, the continuum unit consists of a flexible backbone and two pairs of actuation tendons routed through six 3D-printed rigid spacer disks. We choose an extension spring (3630N321, McMaster-Carr) with a spring rate of 0.832 N/mm as the flexible backbone. Each tendon pair has two coupled tendons, which are wound on a spool and terminated at the end disk. Each spool is actuated by one motor (Dynamixel AX-12 A, ROBOTIS), resulting in equal tendon displacements in opposite directions. The two actuation motors are placed orthogonally on the two sides of the backbone, enabling 2-DoF bending of the backbone.

B. Omnidirectional Docking Mechanism

To enable the docking connector with both manipulation and docking abilities, we propose the idea of “**Grasping as Docking**”, which achieves docking connections through gripper-based grasping. This approach allows a gripper to establish a connection by either grasping another gripper or being grasped by others. The key inspiration comes from the versatility of human hands, which can interlink in various orientations to form

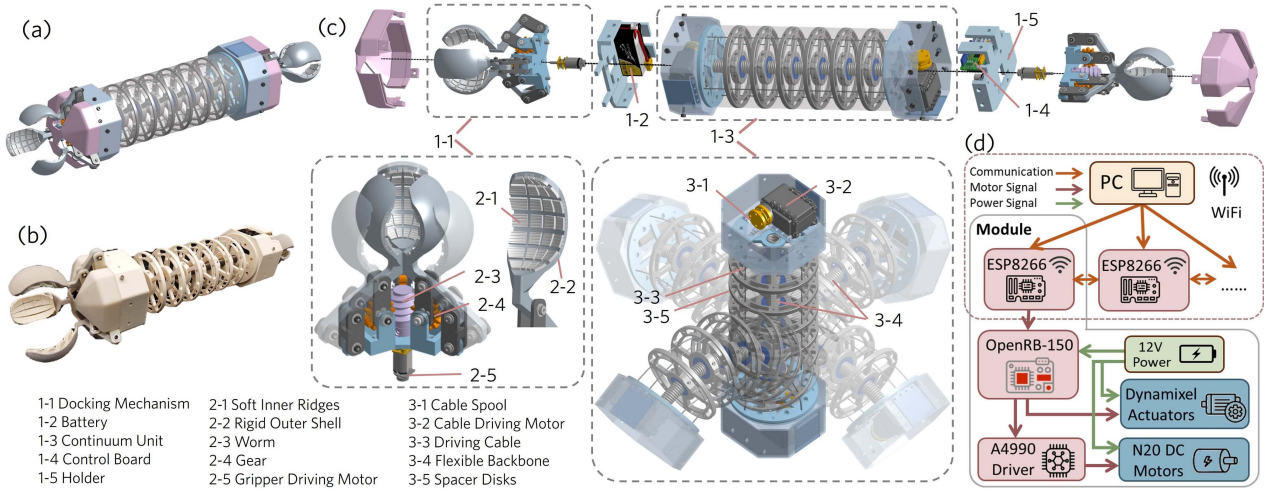


Fig. 2. Design of the MSRCR module. (a) CAD model of a single module. (b) Prototype of a single module. (c) Explored view of the docking mechanism and the continuum unit. (d) Driving mechatronics and communication diagram.

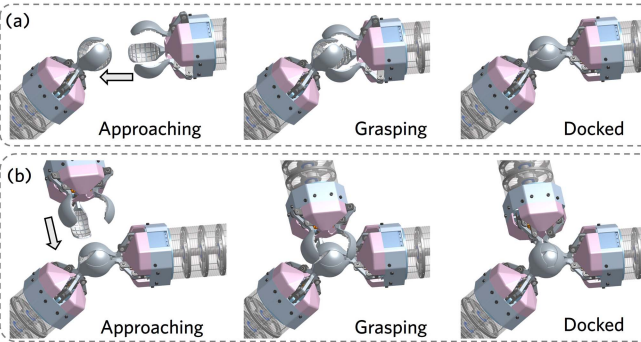


Fig. 3. Principle of the “Grasping as Docking” mechanism. (a) One gripper forms the spherical configuration, while another gripper approaches and grasps it to connect two modules. (b) The third module approaches the two docked module and uses the spherical gripper to create the 3-module configuration.

a unified structure, with each hand serving a dual role—both grasping and being grasped.

Following this idea, we propose a novel spherical gripper-based docking mechanism for omnidirectional module-to-module connections. As shown in Fig. 2(c), the connector features a rigid spherical outer shell, which is divided into three fingers and forms a multi-finger gripper. Each finger is a 90° spherical surface, and there are gaps between fingers to accommodate the base supporting bar of the grippers being grasped. The gripper's motion is driven by a worm-gear mechanism actuated by a N20 DC gear motor (Gear ratio 1000:1, Pololu). Such worm-gear mechanism can prevent the gripper loosing by self-locking. Closing these fingers transforms the connector into a spherical shape, enabling another gripper's inner surface to encase and grasp it from different directions. The closed outer gripper then forms another sphere, allowing additional connectors to securely grasp it (Fig. 3).

To address the diameter disparity caused by the shell's thickness, we propose a hybrid rigid-soft gripper surface design. The gripper has a layer of soft material (TEPU 30 A) embedded on the inner surface of the rigid (Titan Tough Epoxy 85) spherical shell, fabricated in a multi-material additive manufacturing system (Inkbit). The soft ridges enhance the gripper's adaptability to the

TABLE I
SPECIFICATIONS OF EACH MSRCR MODULE

Specifications	Value
Length of the continuum module [mm]	220
Diameter of the continuum module [mm]	90
Max circumcircle diameter of the docking connector [mm]	108.4
Diameter of closed docking gripper [mm]	60
Thickness of the rigid shell in the docking gripper [mm]	2.5
Thickness of the soft ridge in the docking gripper [mm]	1.5
Total length of a single module [mm]	532
Overall weight (including control mechatronics) [g]	912
Total cost per module [USD]	\$234.2

grasped spherical surface, increasing friction between grippers, and ensuring a secure connection. The detailed docking angle and docking number analysis will be given in Section IV-B. The other specifications of the MSRCR module design are summarized in Table I.

C. Electronics and Communication

As shown in Fig. 2(d), the electronics and communication system of the MSRCR centers on the OpenRB-150 (ROBOTIS) microcontroller, which provides velocity and position control to the DC motor N20 and the dynamixel actuators. Using the ESP8266 Wi-Fi module, each module can communicate directly with one another, as well as an external PC that provides commands and monitors status. A customized PCB is designed to integrate Wi-Fi, microcontroller, motor driver, and power supply, enabling the system's untethered versatility.

IV. MODELING AND CHARACTERIZATION

In this section, we provide a kinetostatic model for the continuum unit and also characterize the performance of the docking connector.

A. Kinetostatic Modeling of a Single Module

We rely on the Piecewise Constant Curvature (PCC) assumption to develop the kinetostatic model of continuum unit [33]. Specifically, the segment of the flexible backbone divided by two

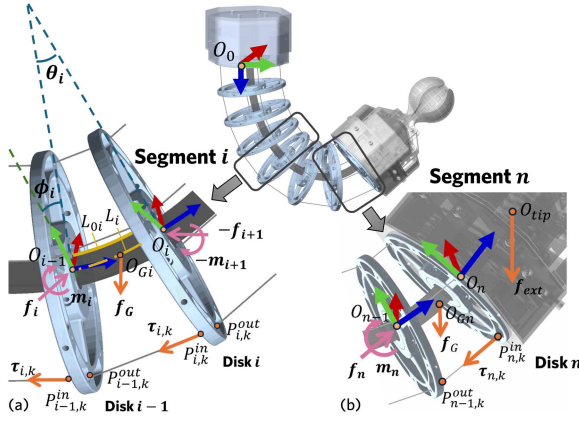


Fig. 4. Kinetostatic modeling of a single module. Diagrams of forces and moments applied to (a) the middle segment i and (b) the tip segment n . (The XYZ axes of the frame are represented by the RGB colors.).

disks is assumed to bend into a continuous constant curvature in space. As shown in Fig. 4, we define the body frame of disk i ($i = 1, \dots, n$) as a frame attached to the center of each disk's distal surface, and the frame 0 is the fixed base frame. The relative rotation between link $i - 1$ and link i is represented by a bending angle θ_i and a bending direction angle ϕ_i . This provides the homogeneous transformation matrix between the two adjacent disks:

$${}^{i-1}\mathbf{T}_i = \begin{bmatrix} {}^{i-1}\mathbf{R}_i & {}^{i-1}\mathbf{t}_i \\ \mathbf{0} & 1 \end{bmatrix} \begin{bmatrix} \mathbf{I} & \mathbf{t}_d \\ \mathbf{0} & 1 \end{bmatrix} \in SE(3) \quad (1)$$

where

$${}^{i-1}\mathbf{R}_i = \mathbf{R}_z(\phi_i) \mathbf{R}_x(-\theta_i) \mathbf{R}_z(-\phi_i) \in SO(3) \quad (2)$$

$${}^{i-1}\mathbf{t}_i = \begin{bmatrix} -\frac{L_i}{\theta_i} \sin(\phi_i)(1 - \cos(\theta_i)) \\ \frac{L_i}{\theta_i} \cos(\phi_i)(1 - \cos(\theta_i)) \\ \frac{L_i}{\theta_i} \sin(\theta_i) \end{bmatrix} \quad (3)$$

where matrices \mathbf{R}_x and \mathbf{R}_z are the rotation matrices that rotate a 3-D vector about the x -axis and y -axis, respectively; $\mathbf{t}_d = [0, 0, L_d]^T$ and L_d is the disk thickness, and L_i is the arc length of the continuum backbone's center line. Since we used an extension spring with stacked coils as a backbone, the coils on the side opposite the bending direction will separate from each other, leading to an increase in the arc length. Such passive extension differs from previous work on continuum robot. We can describe the arc length of the spring's center line as:

$$L_i = L_{i0} + r_b \theta_i \quad (4)$$

where L_{i0} is the unbent length of the segment i and r_b is the radius of the backbone.

The homogeneous transformation matrix between link i and the world frame is given by:

$$\mathbf{T}_i = \mathbf{T}_0 \prod_{j=1}^i {}^{j-1}\mathbf{T}_j \in SE(3) \quad (5)$$

where the \mathbf{T}_0 is the transformation matrix between the world frame and the base frame.

The k^{th} tendon ($k = 1, 2, 3, 4$) passes into and out of the disk i at the points $P_{i,k}^{in}$ and $P_{i,k}^{out}$, respectively. These two points are

expressed in the body frame of link i as:

$$\begin{aligned} {}^b P_{i,k}^{out} &= \left[r_t \cos\left(\frac{\pi}{2}(k-1)\right), r_t \sin\left(\frac{\pi}{2}(k-1)\right), 0 \right]^T \\ {}^b P_{i,k}^{in} &= {}^b P_{i,k}^{out} - [0, 0, L_d]^T \end{aligned} \quad (6)$$

where r_t is the distance between the channel center and the disk center. Using the transformation matrix \mathbf{T}_i , we can transform ${}^b P_{i,k}^{out}$ and ${}^b P_{i,k}^{in}$ into the world frame as $P_{i,k}^{out}$ and $P_{i,k}^{in}$. Next, we will consider the force and moment applied to each segment in the world frame.

As shown in Fig. 4, the force equilibrium equation of the tip segment can be expressed as:

$$\sum_{k=1}^4 \boldsymbol{\tau}_{n,k} + \mathbf{f}_G + \mathbf{f}_{ext} + \mathbf{f}_n = \mathbf{0} \quad (7)$$

where $\boldsymbol{\tau}_{n,k} = F_k (\overrightarrow{P_{n,k}^{in} P_{n-1,k}^{out}} / \| \overrightarrow{P_{n,k}^{in} P_{n-1,k}^{out}} \|)$ is the tension force of the tendon k , \mathbf{f}_G is the gravity force of the segment, \mathbf{f}_{ext} is the external load applied on the tip disk, and \mathbf{f}_n is the interaction force applied by segment $n - 1$ to segment n at O_{n-1} . Here we ignore the tension loss caused by friction as in [34].

The moment equilibrium equation of the tip segment is:

$$\sum_{k=1}^4 \mathbf{m}_{n,k} + \mathbf{m}_G + \mathbf{m}_{ext} + \mathbf{m}_n = \mathbf{0} \quad (8)$$

where $\mathbf{m}_{n,k} = \overrightarrow{O_{n-1} P_{n,k}^{in}} \times \boldsymbol{\tau}_{n,k}$ is the moment caused by tendon tension, $\mathbf{m}_G = \overrightarrow{O_{n-1} O_{Gn}} \times \mathbf{f}_G$ is the moment caused by segment's gravity, and the $\mathbf{m}_{ext} = \overrightarrow{O_{n-1} O_{tip}} \times \mathbf{f}_{ext}$ is the moment caused by the load on the tip disk, and \mathbf{m}_n is the moment applied by segment $n - 1$ to the segment n .

Similarly, we can derive the force and moment equilibrium equations for the middle segment i as:

$$\sum_{k=1}^4 (\boldsymbol{\tau}_{i,k} - \boldsymbol{\tau}_{i+1,k}) + \mathbf{f}_G + \mathbf{f}_i - \mathbf{f}_{i+1} = \mathbf{0} \quad (9)$$

$$\sum_{k=1}^4 \mathbf{m}_{i,k} + \mathbf{m}_G - \overrightarrow{O_{i-1} O_i} \times \mathbf{f}_{i+1} + \mathbf{m}_i - \mathbf{m}_{i+1} = \mathbf{0} \quad (10)$$

where $\mathbf{m}_{i,k} = \overrightarrow{O_{i-1} P_{i,k}^{in}} \times \boldsymbol{\tau}_{i,k} - \overrightarrow{O_{i-1} P_{i+1,k}^{out}} \times \boldsymbol{\tau}_{i+1,k}$ is the net moment applied by the tendon tension passing through disk i . By recursively solving equations (7)–(10), we can get the pure moment \mathbf{m}_i that causes the applied to each segment to bend.

Therefore, given the constitutive law of each segment, the following equation can be obtained for segment i :

$$\mathbf{m}_i = \mathbf{R}_z(\phi_i) \mathbf{R}_{i-1} [\mathcal{F}(\theta_i) \ 0 \ 0]^T \quad (11)$$

where \mathbf{R}_{i-1} is the rotational component (submatrix) of the homogeneous transformation matrix \mathbf{T}_{i-1} . $\mathcal{F}(\theta_i)$ represents the bending moment that is a function of the bending angle, which we experimentally calibrate in Section V-A.

Since we control the robot by tendon displacement instead of the tendon tension, an additional constraint equation is required that relates the tension τ to the displacement l_k^q considering the tendon stretch.

$$l_k^q + l_k^B - l_{k,0}(1 + c\tau_k) = 0 \quad (12)$$

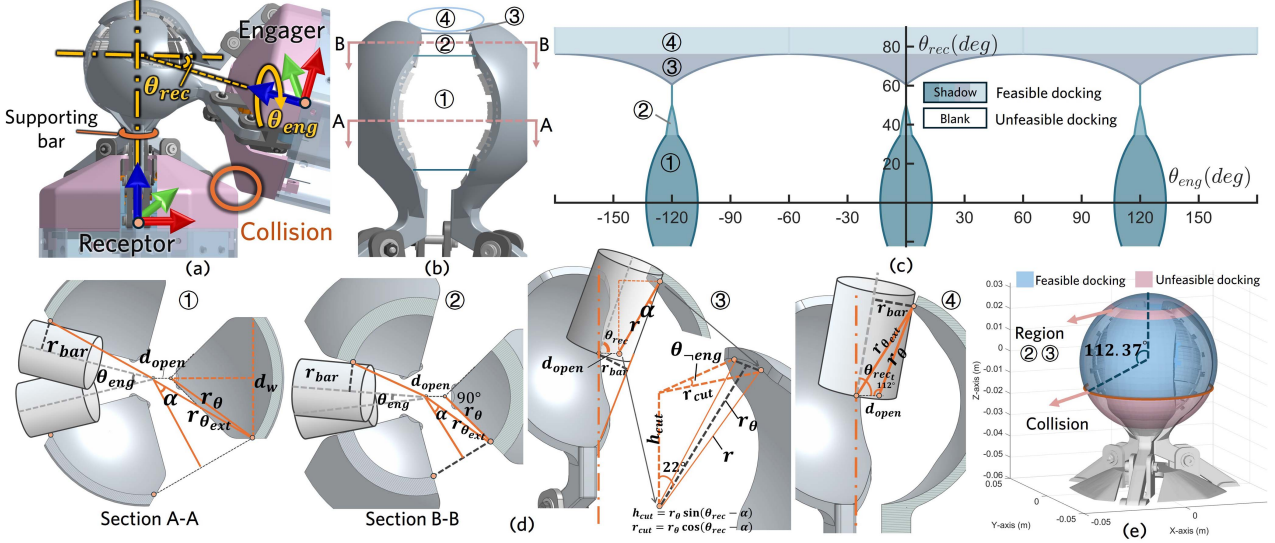


Fig. 5. Docking angle analysis. (a) Docking angle definition between receptors and engagers. (b) Region division of the gap between gripper fingers. (c) Feasible docking range described by $(\theta_{rec}, \theta_{eng})$. (d) Geometrical relationship between θ_{rec} and θ_{eng} . (e) Feasible docking range on a receptor's surface.

where $l_{k,0}$ is the initial unstretched length of tendon k , l_k^B is the tendon length found by summing of the tendon segments along the backbone, and c is the tendon compliance. The slackening tendons with zero tension are not considered.

Given the tendon displacement $\mathbf{l}^q = [l_1^q, \dots, l_4^q]$ and the world-to-base transformation matrix \mathbf{T}_0 , the forward kinematics can be obtained by solving equations (1)–(12) to determine the poses of all the disks. The position of any point along the backbone can also be determined by introducing a scalar parameter $\xi \in [0, 1]$ from the proximal ($\xi = 0$) to the distal end ($\xi = 1$) [35], which is represented as $p(\mathbf{T}_0, \mathbf{l}^q, \xi)$. Inverse kinematics can be formulated as minimizing the error between $p(\mathbf{T}_0, \mathbf{l}^q, \xi)$ and a target position to find the optimal actuation length and, if necessary, the base pose.

B. Docking Angle Analysis

To analyze the feasible docking angle of the proposed docking gripper, we refer to the gripper being grasped as the “Receptor” and the gripper engaging with it as the “Engager” as illustrated in Fig. 5(a). Two angles define the feasible docking range: θ_{rec} represents the polar angle of the receptor’s connection direction, while θ_{eng} denotes the azimuthal docking range of the receptor around its z-axis. The receptor is capable of being connected from any azimuthal direction.

As described in Section III-B, the gripper fingers have gaps between each other that allow the receptor’s base supporting bar to pass through. Based on geometric design, these gaps are divided into four regions, labeled ① - ④ as shown in Fig. 5(b). Fig. 5(c) describes the feasible docking angle pair $(\theta_{rec}, \theta_{eng})$ in the four gap regions, which is based on the geometrical analysis in Fig. 5(d). The relationship between θ_{rec} and θ_{eng} is calculated as:

$$\theta_{eng} = \begin{cases} 2(\alpha - \arcsin \frac{r_{bar}}{r_{\theta_{ext}}}), & \text{Region } ①, ② \\ \frac{2\pi}{3} - 2 \arccos \left(\frac{\tan 22^\circ}{\tan(\theta_{rec} - \alpha)} \right), & \text{Region } ③ \\ 2\pi, & \text{Region } ④ \end{cases} \quad (13)$$

where

$$\alpha = \begin{cases} \frac{\pi}{3} - \arcsin \left(\frac{0.5d_w}{r_{\theta_{ext}}} \right), & \text{Region } ① \\ \frac{\pi}{3} - \arcsin \frac{r_{\theta} \sin(5\pi/4)}{r_{\theta_{ext}}}, & \text{Region } ② \\ \arcsin \left(\frac{r_{bar}}{r} \tan \theta - \frac{d_{open}}{r} \sin \theta \right), & \text{Region } ③ \end{cases}$$

$$r_{\theta_{ext}} =$$

$$\begin{cases} \left((d_w/2)^2 + \left(d_{open} + \sqrt{r_{\theta}^2 - (d_w/2)^2} \right)^2 \right)^{1/2}, & \text{Region } ① \\ (d_{open}^2 + r_{\theta}^2 - 2d_{open}r_{\theta} \cos(5\pi/4))^{1/2}, & \text{Region } ② \end{cases}$$

where d_{open} is the opening distance of the engager gripper, and r_{bar} is the radius of the supporting bar, and $r_{\theta} = r \cos \theta_{rec}$ and r is the gripper radius. Other notations are illustrated in Fig. 5(d). The transition θ_{rec} between region ③ and ④ is determined by

$$\theta_{rec_t} = \arcsin \left(r_{\theta}/r_{\theta_{ext_t}} \sin 112^\circ \right) + \arcsin \left(r_{bar}/r_{\theta_{ext_t}} \right)$$

where

$$r_{\theta_{ext_t}} = \sqrt{r_{\theta}^2 + d_{open}^2 - 2r_{\theta}d_{open} \cos 112^\circ}$$

As shown in Fig. 5(e), with a typical opening distance of 5.7 mm for docking grasping, 56.64% of the receptor’s surface is within the feasible docking range. The infeasible region is mainly due to the neck of region ②③ and potential collision of the connector’s base. Similar analysis applies to the docking of more than two modules. The proposed design allows up to four modules docking at a single node simultaneously.

It should be noted that to ensure a successful docking, the engager should approach the receptor at the correct docking angle and maintain a firm grasp throughout the motion. Once the receptor is securely docked, relative rotation between the receptor and the engager is not allowed. To adjust the docking angle, the engager must undock and approach from a different θ_{rec} and θ_{eng} before actual engaging.

The gripper’s strength was tested by assessing its ability to securely hold an object under external forces. Results show that

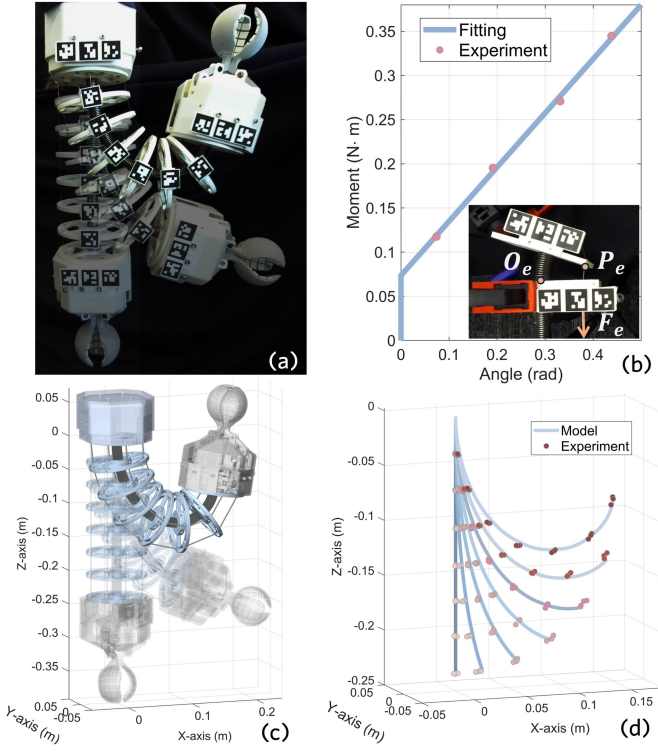


Fig. 6. Kinetostatic model verification. (a) Experimental setup and the robot shape under the actuation length of 0, $3\pi r_{act}$, $6\pi r_{act}$. (b) Bending stiffness calibration of the flexible backbone. (c) Model prediction of the robot shape under the same actuation length as (a). (d) Comparison of model prediction and experiment data over 3 trials.

the gripper can withstand an axial force of 25.35 N, a lateral force of 21.77 N (larger than twice the weight of a single module), and a torque of 0.65 Nm, while maintaining a secure grip, ensuring sufficient strength for docking with other modules. Details can be found in the supplementary video.

V. RESULTS AND DEMONSTRATION

A. Kinetostatic Model Validation

We first experimentally verified the proposed kinetostatic model. As shown in Fig. 6(a), Aruco markers are attached to a single module to measure its pose after bending. We collected seven bent shapes by actuating the tendon length l_1^q from 0 to $6\pi r_{act}$ at a step of πr_{act} , where $r_{act} = 6.5$ mm is the radius of the actuation spool.

We calibrated the bending stiffness of the extension spring used as the flexible backbone. As shown in Fig. 6(b), by applying pure tension \mathbf{F}_e , the pure moment applied to a segment of flexible backbone is $\mathbf{M} = \overrightarrow{O_e P_e} \times \mathbf{F}_e$, and the relationship between \mathbf{M} and bending angle θ is:

$$\|\mathbf{M}\| = \mathcal{F}(\theta) = 0.613\theta + 0.074 \quad (14)$$

The constant term in $\mathcal{F}(\theta)$ is induced by the pre-tension of the extension spring used as the flexible backbone. We also calibrated the tendon compliance c using the robot shape with a tendon actuation length of $4.5\pi r_{act}$ and obtained that $c = 8.64 \times 10^{-3} \text{ N}^{-1}$. Note that the robot shape used for fitting is not included in the testing samples. Fig. 6(d) shows that the model predicts the experiment data well, with an average tip

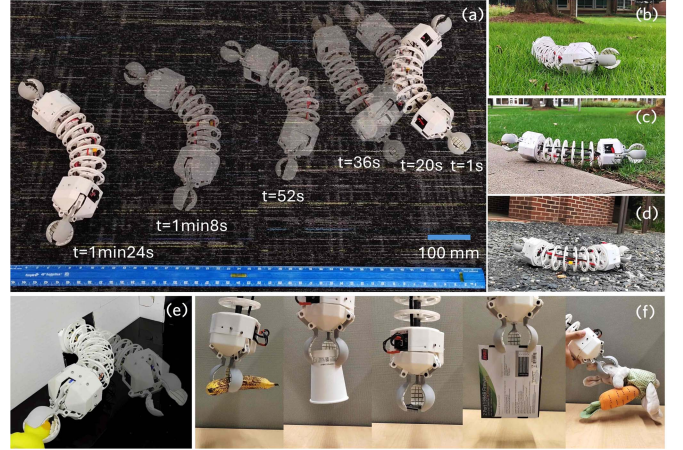


Fig. 7. Single module locomotion and manipulation. (a-d) Single module rolling-based locomotion on smooth carpet, grass, transitioned terrains, and cobblestone. (e) Manipulation of single module for a narrow entrance and confined space. (f) Single module grasping objects with different shapes and sizes, including a banana, a cup, an electronic chip, a box, and a soft toy.

error of 3.41 mm (1.45% of the total length). Fig. 6(c) shows the model prediction of the robot shape under the actuation length of 0, $3\pi r_{act}$, $6\pi r_{act}$, which fits well with the experiment shapes in Fig. 6(a).

B. Single Module Locomotion and Manipulation

1) Rolling: A single module is capable of locomotion on the ground using a rolling gait. Since gravity is fully canceled during rolling, we further simplify the PCC assumption to a constant curvature assumption that all the segments have the same bending angle. We denote the bending angle of the entire robot as $\Theta = n\theta$ and the bending direction as $\Phi = n\phi$. The targeted rolling motion gait in one period T is described by:

$$\Theta(t) = \Theta_0, \quad \Phi(t) = 2\pi t/T + \Phi_0 \quad (t \in [0, T]) \quad (15)$$

The target backbone pose can be derived by substituting (15) into (1)-(5), and the actuation length l^q is then computed through inverse kinematics. This rolling motion involves continuously changing the bending direction from 0 to 360° , which employs the same tendon actuation that enables the robot tip to trace a circular path when the robot base is fixed. In rolling motion, however, the bending plane rotates around the base frame's z -axis while remaining aligned with the ground plane, causing the base and all disks to rotate on the ground.

As shown in Fig. 7(a), a single module can roll on a smooth carpet at a speed of 13.54 mm/s (1.52 body length/min). It is also able to traverse through different terrains, including grass, cobblestone, cement road and terrain transitions (Fig. 7(b-d)). This single module rolling speed exceeds many related works [4], [6], [32] but is slower than some [5], [8], with the potential to increase by easily adjusting the tendon actuation motor speed.

2) Manipulation: The module can also be mounted on a robot arm for the manipulation in confined space. As demonstrated in Fig. 7(e), the module is capable of navigating through a narrow entrance, steering in 3D space, and grasping an object hidden in a corner using the docking gripper. Note that the control is implemented by teleoperation. As shown in Fig. 7(f), we demonstrated the gripper's ability to grasp different objects

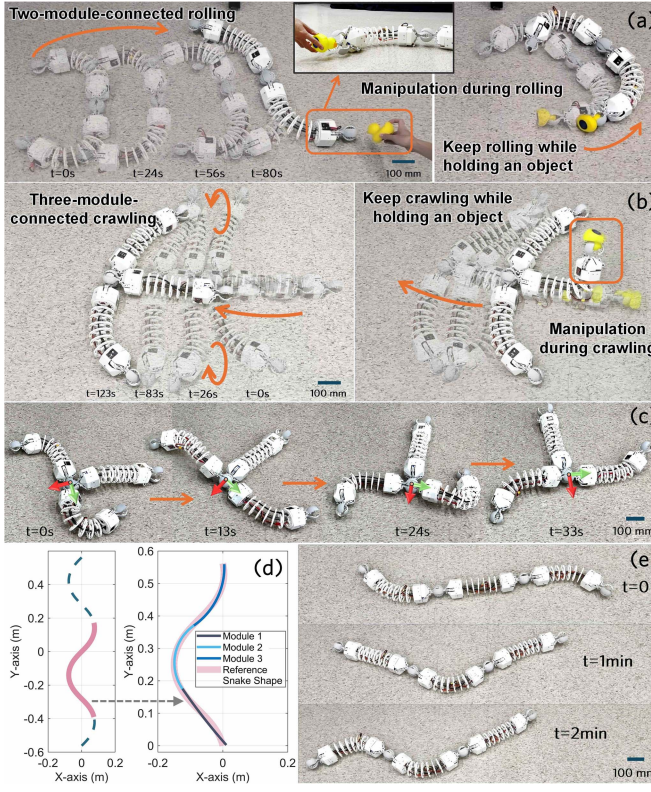


Fig. 8. Multiple module locomotion and manipulation. (a) Rolling and manipulation of two connected modules. (b) Forward crawling and manipulation of three connected modules. (c) Turning of three connected modules. (d) Reference snake undulation trajectory used for three chained modules to track. (e) Snake-like undulation motion.

with various shapes and sizes, highlighting its versatility beyond its primary function as a modular connector.

C. Multiple Module Locomotion and Manipulation

1) *Rolling-Based Loco-Manipulation*: Two connected modules can roll together, with a docking angle of $\theta_{rec} = 90^\circ$. Two modules roll in the opposite directions, which is described by $\Phi_1(t) = \frac{2\pi}{T}t + \Phi_0$ and $\Phi_2(t) = -\frac{2\pi}{T}t + \Phi_0$ and $\Theta_1 = \Theta_2$. As shown in Fig. 8(a), the free-end grippers can be used to manipulate objects during the two-module rolling. The control mode switches from autonomous rolling to teleoperation for manipulation.

2) *Crawling-Based Loco-Manipulation*: With three modules centrally connected, the robot forms a mudskipper-like configuration in which two modules act like “arms” and one module acts like a “tail”. As shown in Fig. 8(b), this configuration enables the robot to crawl forward by swinging the two arms and manipulate objects using the tail gripper during crawling. The two arm modules bend into 45° and use the same rolling gait as the connected rolling motion, while the tail module constrains the rolling of the connection point. Therefore, the free ends of two arms will follow a circular path vertically, pushing the entire robot body up and forward. As shown in Fig. 8(c), by setting the two arm’s rolling gait identically, in-place turning can be achieved.

3) *Snake-Like Undulation*: A snake-like configuration can be formed by connecting three modules in an open chain. To achieve the snake-like undulation, we first plan a reference

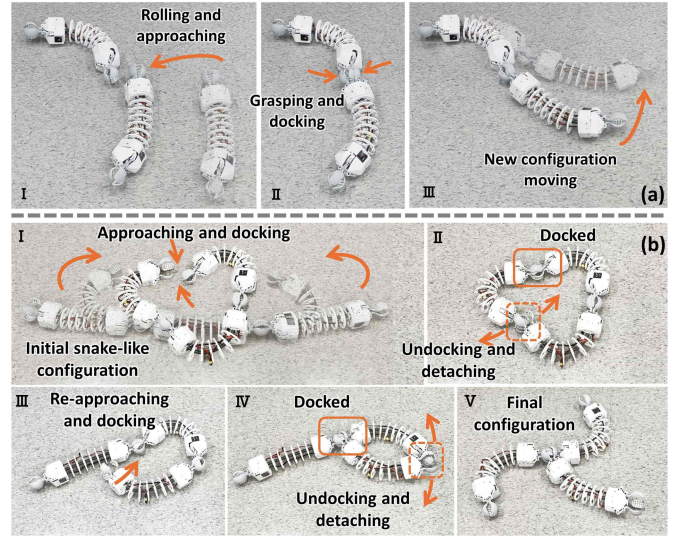


Fig. 9. Demonstration of reconfiguration process. (a) Scaling mode: reconfiguration by adding a module. (b) Shifting mode: Three modules changing from snake-like to crawler configuration.

follow-the-leader motion trajectory as described in [36]:

$$p_{ref}(t, s) = \begin{bmatrix} \int_0^{vt-s} \sin\left(\frac{\pi}{2} - \frac{\pi}{4} \cos\left(\frac{2\pi}{L_{total}}\xi\right)\right) d\xi \\ \int_0^{vt-s} \cos\left(\frac{\pi}{2} - \frac{\pi}{4} \cos\left(\frac{2\pi}{L_{total}}\xi\right)\right) d\xi \end{bmatrix} \quad (16)$$

where L_{total} is the snake length, $s \in [0, L_{total}]$ is the arc length parameter, $v = L_{total}/T$ is the tangent velocity of the snake head over the time period, and p_{ref} defines the 2D position of any point along the snake at time t . To track the reference snake undulation motion, we solve an optimization-based inverse kinematics problem to get the tendon actuation length at time t :

$$\min_{\mathbf{T}_0, \mathbf{l}^q(t)} \sum_{k=1}^{N_{sample}} \|p_{chain}(\mathbf{T}_0, \mathbf{l}^q(t), \xi_k) - p_{ref}(t, s_k)\|^2 \quad (17)$$

where $\xi_k \in [0, 1]$ and $s_k = \xi_k L_{total}$, and p_{chain} defines the forward kinematics of the three sequentially connected modules. L_{total} is the total length of three chained modules, ignoring the length of docking connectors. In this formulation, we minimize the distance between the reference and three chained modules by sampling N_{sample} points along the body (Fig. 8(d)). As shown in Fig. 8(e), three connected modules successfully achieved a snake-like undulation motion and moved leftward using the designed gait.

D. Reconfiguration

We propose two self-reconfiguration modes: (1) *scaling mode*, where the configuration changes by increasing/decreasing the number of modules, and (2) *shifting mode*, where the configuration changes by altering the connections between modules and maintains a constant number of modules.

1) *Scaling Mode*: As shown in Fig. 9(a), one module approaches another (Step I) by rolling, docks with it by grasping (Step II), and transits the system into a two-module configuration that moves as a unified system (Step III).

2) *Shifting Mode*: Unlike Scaling Mode, in Shifting Mode, each module maintains at least one connection with another

module. As shown in Fig. 9(b), starting from an initial snake-like configuration, the three connected modules can shift to a centralized configuration by docking and undocking of connectors. This reconfiguration process provides substantial adaptability for diverse terrains. For instance, the snake-like configuration excels in navigating confined spaces, whereas the centralized configuration is more suited for traversing open spaces.

We also want to emphasize that the current reconfiguration process is controlled by teleoperation. While it is not yet fully autonomous due to the absence of feedback for precise control, our proposed system eliminates the need for manual intervention on-site, achieving complete self-reconfigurability. The detailed loco-manipulation and self-reconfiguration processes are presented in the supplementary video.

VI. CONCLUSIONS AND FUTURE WORK

In this study, we presented a novel modular self-reconfigurable continuum robot designed for general-purpose loco-manipulation tasks. We also demonstrated the self-reconfiguration process and diverse loco-manipulation capabilities with different configurations, opening new possibilities for these adaptive robotic systems.

Several challenges remain in the design and control of the proposed robot system, which will be addressed in future work. First, the onboard sensors used for robot state estimation and environment perception will be integrated into future designs, providing feedback for docking alignment, autonomous navigation, and precise motion control. Second, the current spherical gripper is limited in performing fine manipulation tasks, especially for objects smaller than its inner diameter or thinner than the finger gaps. Future iterations will focus on refining its design for better adaptability and incorporating advanced materials to enhance docking strength. Third, the “task-to-configuration matching” problem will be addressed as the next step, aiming to autonomously transitioning to the optimal configuration for handling diverse application tasks.

REFERENCES

- [1] M. Vespignani, K. Melo, S. Bonardi, and A. J. Ijspeert, “Role of compliance on the locomotion of a reconfigurable modular snake robot,” in *Proc. IEEE/RSJ Int. Conf. Intell. Robots Syst.*, 2015, pp. 2238–2245.
- [2] M. Yim, D. G. Duff, and K. D. Roufas, “PolyBot: A modular reconfigurable robot,” in *Proc. Millennium Conf. IEEE Int. Conf. Robot. Automat. Symposia Proc.*, vol. 1, 2000, pp. 514–520.
- [3] J. Seo, J. Paik, and M. Yim, “Modular reconfigurable robotics,” *Annu. Rev. Control., Robot., Auton. Syst.*, vol. 2, pp. 63–88, 2019.
- [4] S. Li et al., “Scaling up soft robotics: A meter-scale, modular, and reconfigurable soft robotic system,” *Soft Robot.*, vol. 9, no. 2, pp. 324–336, 2022.
- [5] M. E. Sayed, J. O. Roberts, R. M. McKenzie, S. Araci, A. Buchoux, and A. A. Stokes, “Limpet II: A modular, untethered soft robot,” *Soft Robot.*, vol. 8, no. 3, pp. 319–339, 2021.
- [6] J. Zou, Y. Lin, C. Ji, and H. Yang, “A reconfigurable omnidirectional soft robot based on caterpillar locomotion,” *Soft Robot.*, vol. 5, no. 2, pp. 164–174, 2018.
- [7] C. D. Onal and D. Rus, “A modular approach to soft robots,” in *Proc. 4th IEEE RAS EMBS Int. Conf. Biomed. Robot. Biomechatronics*, 2012, pp. 1038–1045.
- [8] Q. Ze et al., “Soft robotic origami crawler,” *Sci. Adv.*, vol. 8, no. 13, 2022, Art. no. eabm7834.
- [9] S. Kurumaya et al., “A modular soft robotic wrist for underwater manipulation,” *Soft Robot.*, vol. 5, no. 4, pp. 399–409, 2018.
- [10] M. A. Robertson and J. Paik, “New soft robots really suck: Vacuum-powered systems empower diverse capabilities,” *Sci. Robot.*, vol. 2, no. 9, 2017, Art. no. eaan6357.
- [11] G. Liang, D. Wu, Y. Tu, and T. L. Lam, “Decoding modular reconfigurable robots: A survey on mechanisms and design,” *Int. J. Robot. Res.*, 2024.
- [12] C. Liu, Q. Lin, H. Kim, and M. Yim, “SMORES-EP, a modular robot with parallel self-assembly,” *Auton. Robots*, vol. 47, no. 2, pp. 211–228, 2023.
- [13] J. Sugihara, T. Nishio, K. Nagato, M. Nakao, and M. Zhao, “Design, control, and motion strategy of trady: Tilted-rotor-equipped aerial robot with autonomous in-flight assembly and disassembly ability,” *Adv. Intell. Syst.*, vol. 5, no. 10, Oct. 2023, Art. no. 2300191.
- [14] V. Zykov, E. Mytilinaios, B. Adams, and H. Lipson, “Self-reproducing machines,” *Nature*, vol. 435, no. 7039, pp. 163/164, 2005.
- [15] C. H. Belke and J. Paik, “Mori: A modular origami robot,” *IEEE/ASME Trans. Mechatron.*, vol. 22, no. 5, pp. 2153–2164, Oct. 2017.
- [16] A. Sproewitz, A. Billard, P. Dillenbourg, and A. J. Ijspeert, “Roombots-mechanical design of self-reconfiguring modular robots for adaptive furniture,” in *Proc. IEEE Int. Conf. Robot. Automat.*, 2009, pp. 4259–4264.
- [17] J. W. Romanishin, K. Gilpin, and D. Rus, “M-blocks: Momentum-driven, magnetic modular robots,” in *Proc. IEEE/RSJ Int. Conf. Intell. Robots Syst.*, 2013, pp. 4288–4295.
- [18] D. Saldaña, B. Gabrich, G. Li, M. Yim, and V. Kumar, “ModQuad: The flying modular structure that self-assembles in midair,” in *Proc. IEEE Int. Conf. Robot. Automat.*, 2018, pp. 691–698.
- [19] G. Liang, H. Luo, M. Li, H. Qian, and T. L. Lam, “FreeBOT: A freeform modular self-reconfigurable robot with arbitrary connection point-design and implementation,” in *Proc. IEEE/RSJ Int. Conf. Intell. Robots Syst.*, 2020, pp. 6506–6513.
- [20] D. Zhao, H. Luo, Y. Tu, C. Meng, and T. L. Lam, “Snail-inspired robotic swarms: A hybrid connector drives collective adaptation in unstructured outdoor environments,” *Nat. Commun.*, vol. 15, no. 1, 2024, Art. no. 3647.
- [21] P. Swissler and M. Rubenstein, “FireAntV3: A modular self-reconfigurable robot towards free-form self-assembly using attach-anywhere continuous docks,” *IEEE Robot. Automat. Lett.*, vol. 8, no. 8, pp. 4911–4918, Aug. 2023.
- [22] Q. Guan, J. Sun, Y. Liu, N. M. Wereley, and J. Leng, “Novel bending and helical extensile/contractile pneumatic artificial muscles inspired by elephant trunk,” *Soft Robot.*, vol. 7, no. 5, pp. 597–614, 2020.
- [23] S. Wu, Q. Ze, J. Dai, N. Udupi, G. H. Paulino, and R. Zhao, “Stretchable origami robotic arm with omnidirectional bending and twisting,” *Proc. Nat. Acad. Sci.*, vol. 118, no. 36, 2021, Art. no. e2110023118.
- [24] S. Abondance, C. B. Teeple, and R. J. Wood, “A dexterous soft robotic hand for delicate in-hand manipulation,” *IEEE Robot. Automat. Lett.*, vol. 5, no. 4, pp. 5502–5509, Oct. 2020.
- [25] Z. Wan et al., “Design, analysis, and real-time simulation of a 3D soft robotic snake,” *Soft Robot.*, vol. 10, no. 2, pp. 258–268, 2023.
- [26] F. Connolly, P. Polygerinos, C. J. Walsh, and K. Bertoldi, “Mechanical programming of soft actuators by varying fiber angle,” *Soft Robot.*, vol. 2, no. 1, pp. 26–32, 2015.
- [27] S. W. Kwok et al., “Magnetic assembly of soft robots with hard components,” *Adv. Funct. Materials*, vol. 24, no. 15, pp. 2180–2187, Apr. 2014.
- [28] D. D. K. Arachchige, D. M. Perera, S. Mallikarachchi, U. Huzaifa, I. Kanj, and I. S. Godage, “Soft steps: Exploring quadrupedal locomotion with modular soft robots,” *IEEE Access*, vol. 11, pp. 63136–63148, 2023.
- [29] D. M. Perera et al., “Teleoperation of soft modular robots: Study on real-time stability and gait control,” in *Proc. IEEE Int. Conf. Soft Robot.*, 2023, pp. 01–07.
- [30] D. D. K. Arachchige, Y. Chen, and I. S. Godage, “Soft robotic snake locomotion: Modeling and experimental assessment,” in *Proc. IEEE 17th Int. Conf. Automat. Sci. Eng.*, 2021, pp. 805–810.
- [31] D. D. K. Arachchige, Y. Chen, I. D. Walker, and I. S. Godage, “A novel variable stiffness soft robotic gripper,” in *Proc. IEEE 17th Int. Conf. Automat. Sci. Eng.*, 2021, pp. 2222–2227.
- [32] L. Zhao et al., “StarBlocks: Soft actuated self-connecting blocks for building deformable lattice structures,” *IEEE Robot. Automat. Lett.*, vol. 8, no. 8, pp. 4521–4528, Aug. 2023.
- [33] P. Rao, Q. Peyron, S. Lilge, and J. Burgner-Kahrs, “How to model tendon-driven continuum robots and benchmark modelling performance,” *Front. Robot. AI*, vol. 7, 2021, Art. no. 630245.
- [34] D. C. Rucker and R. J. Webster III, “Statics and dynamics of continuum robots with general tendon routing and external loading,” *IEEE Trans. Robot.*, vol. 27, no. 6, pp. 1033–1044, Dec. 2011.
- [35] M. Azizkhani, I. S. Godage, and Y. Chen, “Dynamic control of soft robotic arm: A simulation study,” *IEEE Robot. Automat. Lett.*, vol. 7, no. 2, pp. 3584–3591, Apr. 2022.
- [36] J. Ha, “Robotic snake locomotion exploiting body compliance and uniform body tensions,” *IEEE Trans. Robot.*, vol. 39, no. 5, pp. 3875–3887, Oct. 2023.